On the Response of a Buoyant Plume to Downwelling-Favorable Wind Stress

CARLOS MOFFAT

Departamento de Oceanografía, Universidad de Concepción, Concepción, Chile

STEVEN LENTZ

Department of Physical Oceanography, Woods Hole Oceanographic Institution, Woods Hole, Massachusetts

ABSTRACT

Here, the response of a coastally trapped buoyant plume to downwelling-favorable wind forcing is explored using a simplified two-dimensional numerical model and a prognostic theory for the resulting width, depth, and density anomaly and along-shelf transport of the plume. Consistent with the numerical simulations, the analytical model shows that the wind causes mixing of the plume water and that the forced cross-shelf circulation can also generate significant deepening and surface narrowing, as well as increased along-shelf transport. The response is due to a combination of the purely advective process that leads to the steepening of the isopycnals and the entrainment of ambient water into the plume. The advective component depends on the initial plume geometry: plumes that have a large fraction of their total width in contact with the bottom ("bottom trapped") suffer relatively small depth and width changes compared to plumes that have a large fraction of their total width detached from the bottom ("surface trapped"). Key theoretical parameters are W_γ/W_α, the ratio of the width of the plume detached from the bottom to the width of the plume in contact with it, and the ratio of the wind-generated mixed layer δ_e to the initial plume depth h_p, which determines the amount of water initially entrained into the plume. The model results also show that the cross-shelf circulation can be strongly influenced by the wind-driven response in combination with the geostrophic shear of the plume. The continuous entrainment into the plume, as well as transient events, is also discussed.

1. Introduction

River discharge is a key component of the circulation and property budgets of the coastal ocean. The freshwater output can be a fundamental component of the salt budget of the shelf. Sediment (Ogston et al. 2000; Geyer et al. 2000), nutrients (Kudela et al. 2008), and pollutants collected in the river basin have a significant impact on biological productivity (Hickey et al. 2010) and the environmental quality of coastal waters (Wang 2006). Coastally trapped buoyant plumes have been observed to propagate for long distances along the coast (Rennie et al. 1999; Lentz and Largier 2006; Warrick et al. 2007; Hickey et al. 2010) and thus provide an effective mechanism for the alongshore transport of freshwater, as well as dissolved and suspended material in the buoyant water.

The circulation of the river outflow on the shelf is strongly influenced by its buoyancy, rotational effects, and the presence of a lateral boundary. Observations of these systems reveal that, upon exiting the river mouth, the flow rotates anticyclonically. In this near-field region, an expanding bulge is sometimes observed (Horner-Devine 2009), but numerical models results suggest its formation can be frequently inhibited—and thus less frequently observed—by the common occurrence of alongshore ambient flows (e.g., Fong and Geyer 2001). As the input of freshwater continues, the rotating fluid encounters the coastal boundary and forms a coastally trapped, buoyant plume propagating with the coast to its left (right) in the Southern (Northern) Hemisphere (Chao and Boicourt 1986; Wiseman and Garvine 1995). Theory, laboratory experiments, and numerical models (Chapman and Lentz 1994; Kourafalou et al. 1996; Lentz and Helfrich 2002) suggest that the influence of bottom friction is a critical factor in determining its depth and width. In turn, the geometry of the plume helps to determine its propagation speed, with "bottom trapped"

Corresponding author address: Carlos Moffat, Departamento de Oceanografía, Universidad de Concepción, Concepción, Chile.
E-mail: cmoffat@oceanografia.udec.cl

plumes propagating slower than "surface trapped" plumes with the same alongshore transport and density anomaly (Yankovsky and Chapman 1997; Lentz and Helfrich 2002).

However, a number of processes can alter the continuous along-shelf propagation of river plumes. In particular, wind stress forcing has been shown to strongly affect their propagation and coherence. When forced by upwelling-favorable wind stress, field observations show the plumes becoming wider and thinner as a result of the generated cross-shore Ekman circulation (Rennie et al. 1999; Lentz et al. 1999; Hickey et al. 2005). The response to upwelling-favorable winds is unsteady, so that under continuing wind stress forcing the plume eventually separates from the coast and mixes away as it is advected farther offshore. Numerical model results and a two-dimensional theory (Fong and Geyer 2001; Lentz 2004) used to understand the response to upwelling-favorable wind stress show that both offshore advection by the Ekman circulation and entrainment of ambient water into the plume are critical to understand the evolution of the plume geometry and its density anomaly.

A similar, simplified theory of the response of a coastally trapped buoyant plume subjected to downwelling-favorable wind stress is lacking. Observations show that the response is characterized by narrowing and deepening of the plume (Hickey et al. 2005; Rennie et al. 1999), as well as the reduction of the plume stratification as the result of mixing and the steepening of the plume isopycnals (Rennie et al. 1999). The response also results in the intensification of the alongshore plume transport through the steepening of the isopycnals and onset of a barotropic, wind-driven circulation (Lentz 2004; Whitney and Garvine 2005). However, prognostic estimates of the resulting along-shelf transport, as well as the depth, width, and buoyancy deficit of the plume, are needed in order to make progress toward a general model of wind-driven forcing of river plumes.

Here we use a two-dimensional coastal numerical model with simplified (constant slope) bathymetry, initialized with an adjusted buoyant plume and forced by constant, downwelling-favorable wind stress, to explore the dynamics of these plumes under a variety of initial and forcing conditions. This idealized approach allows us to focus on the region of the plume far from the river mouth and the plume nose, in both of which a number of complex processes (e.g., estuarine circulation and plume propagation) are expected to play an important role in setting the plume geometry and hydrographic structure. Section 2 describes a theory for the response, and section 3 describes a two-dimensional numerical model used to explore the plume dynamics and test the theory. The results are discussed in section 4, and, finally, a summary of the results is presented in section 5.
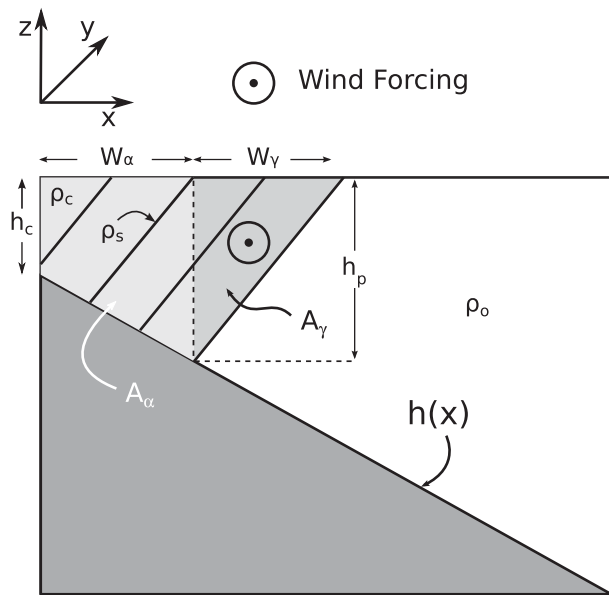

FIG. 1. Schematic of the model geometry and initial conditions. The plume is initialized on a shelf with a vertical wall of depth h_c (5 m) at the coast, a constant bottom slope, and constant density ρ_o. After initial adjustment the plume depth is h_p and its total width is $W_p = W_\alpha + W_\gamma$ with areas A_α (light shading) and A_γ (dark shading). The density anomaly of the plume is $\Delta\rho_c = \rho_o - \rho_c$.

2. Theory

Consider a stratified buoyant plume moving along the coast. The right-handed coordinate system is defined with x positive offshore and z positive upward, with zero at the undisturbed sea surface. The total width of the plume is $W_p = W_\alpha + W_\gamma$, split between an onshore portion in direct contact with the bottom (W_α) and an offshore frontal region (W_γ). The plume depth h_p is the depth of the plume at $x = W_\alpha$. The bathymetry consists of a small vertical wall h_c at the coast and the depth increasing offshore with a constant slope α. Figure 1 shows a schematic of this initial setup.

The theory is two dimensional and it assumes an initial density field with constant vertical and lateral gradients,

$$\rho = \rho_c + \frac{\Delta\rho_c}{W_p}\left(x - \frac{z}{\gamma}\right), \qquad (1)$$

where ρ_c is the surface density at the coast, $\gamma = h_p/W_\gamma$ is the isopycnal slope, and $\Delta\rho_c = \rho_o - \rho_c$ is the density anomaly of the plume with ρ_o the ambient density.

a. Initial plume scales

First, we develop the scalings for the initial geometry (width and depth) and along-shelf transport of the plume,

assuming the plume has reached a steady state where the cross-shore momentum balance is geostrophic and the velocity at the bottom (and thus the bottom stress) is zero (Chapman and Lentz 1997; Lentz and Helfrich 2002). The width of the plume front W_γ can be approximated by the scale (Gill 1976)

$$W_\gamma \sim \frac{(g'_\gamma h_p)^{1/2}}{f} \qquad (2)$$

in which $g'_\gamma = g(\rho_o - \rho_s)/\rho_o$ is the reduced gravity associated with the front and ρ_s is the surface density at $x = W_\alpha$ (Fig. 1). To develop our theory in terms of the overall density difference found in the plume, we take advantage of the constant lateral density difference assumption to rewrite g'_γ as

$$g'_\gamma = \frac{W_\gamma}{W_p} g', \qquad (3)$$

where $g' = g\Delta\rho_c/\rho_o$ is the reduced gravity of the plume. Replacing Eq. (3) in Eq. (2) and solving for W_γ, we obtain a quadratic equation with solution (only the positive root gives a positive width)

$$W_\gamma = \frac{W_\alpha}{2}\left[\left(1 + \frac{4\lambda^2}{W_\alpha^2}\right)^{1/2} - 1\right], \qquad (4)$$

where $\lambda^2 = g'h_p/f^2$ is an internal radius of deformation squared. Notice, however, that the similarly defined deformation radius in Eq. (2) is a more physically relevant scale for this problem.

   Another important property associated with a buoyant plume is the along-shelf transport and how it is related to the plume geometry and buoyancy deficit. We can start with the alongshore vertical shear in the plume, given by

$$\frac{\partial v}{\partial z} = \frac{g}{f\rho_o}\frac{\partial\rho}{\partial x}. \qquad (5)$$

Integrating the equation above and assuming that the alongshore velocity is zero at the bottom for the area A_α [i.e., $v(x, h_\alpha) = 0$] and that the velocity vanishes along the frontal boundary for the area A_γ [i.e., $v(x, h_\gamma) = 0$], we obtain

$$v(z) = \frac{g}{f\rho_o}\frac{\Delta\rho_c}{W_p}(h + z), \qquad (6)$$

which, integrated over the area of the plume, results in the along-shelf transport, given by

$$\begin{aligned} Q_g &= \int_0^{W_p}\int_{-h}^0 v\,dz\,dx \\ &= \frac{g'}{fW_p}\left[\int_0^{W_\alpha}\int_{-h_\alpha}^0 (h_\alpha + z)\,dz\,dx + \int_{W_\alpha}^{W_p}\int_{-h_\gamma}^0 (h_\gamma + z)\,dz\,dx\right] \\ &= \frac{g'}{6f}\left[h_p^2 + h_c\frac{W_\alpha}{W_p}(h_c + h_p)\right] \\ &= \frac{g'h_p^2}{6f}\left[1 + \frac{h_c}{\alpha W_p}\left(1 - \frac{h_c^2}{h_p^2}\right)\right], \end{aligned} \qquad (7)$$

where $h_\alpha(x) = h_c + \alpha x$ is the bottom depth and $h_\gamma(x) = h_p (W_p - x)/W_\gamma$ is the depth of the front offshore of W_α, assuming a triangular shape (Fig. 1). We can readily solve for the depth of the plume:

$$\begin{aligned} h_p &= \left[\frac{6Q_g f}{g'} + h_c^2\left(\frac{1}{4}\frac{1}{(1 + W_\gamma/W_\alpha)^2} - \frac{1}{(1 + W_\gamma/W_\alpha)}\right)\right]^{1/2} \\ &\quad - \frac{h_c}{2}\frac{1}{(1 + W_\gamma/W_\alpha)} \end{aligned} \qquad (8)$$

or

$$h_p = \left(\frac{6Q_g f}{g'}\right)^{1/2} \quad \text{for} \quad h_c = 0. \qquad (9)$$

Note that the chosen bathymetry, with a vertical wall h_c at the coast, results in a more complex expression that requires the details of the plume geometry, instead of simply its transport and reduced gravity. This bathymetry, however, was chosen to accurately judge the numerical model results that we will present in the next section. However, here and throughout the manuscript we also present expressions with h_c set to zero, as they are more relevant for discussion and application to observational studies. Note also that the expression for the plume depth for this problem (with $h_c = 0$ and constant stratification) differs only by a factor of $\frac{1}{3}$ from the estimation of the depth for a plume with a narrow front (Lentz 2004; Avicola and Huq 2003; Pimenta et al. 2011).

b. Response to downwelling-favorable wind stress forcing

   We now turn our attention to the response of the plume to the onset of wind stress forcing. We assume that the wind is constant and downwelling favorable. In this simplified theory, the wind stress acts to modify the plume geometry and buoyancy anomaly through two mechanisms considered here sequentially. First, it creates a surface mixed layer that quickly entrains ambient water

into the plume and steepens the isopycnals within the mixed layer (Fig. 2, top). In a second stage, the spinup of a cross-shelf Ekman circulation advectively steepens the interior isopycnals. Entrainment of ambient water into the plume after the initial formation of the mixed layer is neglected in the theory. The advective steepening is assumed to continue until the isopycnals are essentially vertical (Fig. 2). Below, we derive expressions for the final scales that depend only on the initial conditions and the strength of the wind forcing.

Initially, the wind stress forcing results in the rapid formation of a mixed layer whose depth can be approximated as (Pollard et al. 1972; McWilliams et al. 2009)

$$\delta_e = \frac{1}{(Nf)^{1/2}}\left(\frac{\tau}{\rho_0}\right)^{1/2}, \qquad (10)$$

where δ_e is the depth of the wind-forced Ekman layer and $N^2 = g'/(\gamma W_p)$ is the initial plume stratification. The formation of this layer leads to the entrainment of ambient water into the plume (Fig. 2). Thus, if we consider the area of the frontal portion of the plume prior to the onset of wind forcing, that is,

$$A_\gamma = \frac{1}{2}W_\gamma h_p, \qquad (11)$$

we can write an expression for the area offshore of W_α immediately after the mixed layer has formed:

$$A_{\gamma e} = \begin{cases} \frac{1}{2}\left(W_\gamma h_p + \frac{\delta_e^2}{\gamma}\right) & \text{for} \quad \delta_e < h_p \\ \frac{1}{2}\left(W_\gamma(h_f + h_p) - \frac{(h_f - \delta_e)^2}{\alpha}\right) & \text{for} \quad h_p \leq \delta_e \leq h_f \end{cases},$$

$$(12)$$

where

$$h_f = h_c + \alpha(W_\alpha + W_\gamma) \qquad (13)$$

$$= h_p\left(1 + \frac{\alpha}{\gamma}\right) \qquad (14)$$

is the bottom depth at the outer edge of the plume ($x = W_p$). Thus, when the wind-generated mixed layer is shallower than the initial plume depth, the entrained area is only a function of the Ekman layer depth and the initial isopycnal slope, and therefore a weaker isopycnal slope leads to relatively more ambient water entrained into the plume. For the same plume stratification and depth prior to the onset of the wind, a steeper bottom slope results in stronger mixing of the plume if the wind is strong enough, that is, for $\delta_e > h_p$. Together with the wind stress intensity, the local bathymetry below the
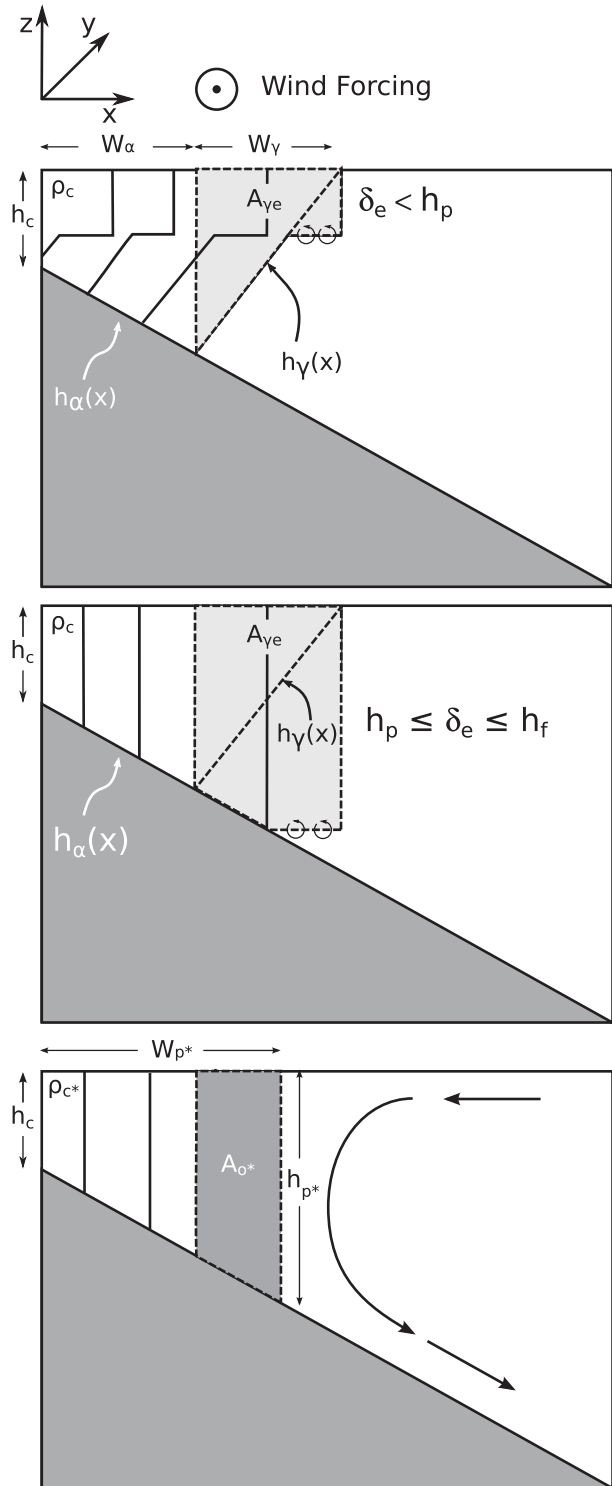

FIG. 2. Schematic of the theoretical evolution of the response to downwelling-favorable wind stress. Initially ambient water is entrained into the plume in a layer of thickness δ_e that can be (top) shallower or (middle) deeper than the initial plume depth h_p. The entrainment expands the initial frontal area to $A_{\gamma e}$. (bottom) Advective steepening leads to vertical isopycnals and the final depth h_{p*}, width W_{p*}, and density anomaly $\rho_o - \rho_{c*}$. In this final state $A_{o*} = A_{\gamma e}$.

plume front determines the total amount of ambient water that can be initially entrained into the plume. The theory predicts that the maximum entrainment will occur when the wind stress is $\tau_m = \rho_o(h_c + \alpha W_p)^2(Nf)$. Increasing the wind intensity above this value would not result in additional entrainment of ambient water, although, as we will see later, stronger winds do affect the plume in other, key ways. However, note that

$$\frac{\alpha}{\gamma} = \frac{W_\gamma}{W_\alpha}\left(1 - \frac{h_c}{h_p}\right) \qquad (15)$$

so that, when $h_c \ll h_p$, $\alpha/\gamma \approx W_\gamma/W_\alpha$ and so Eq. (14) suggests that for bottom-trapped plumes ($W_\gamma/W_\alpha \ll 1$), $h_f \approx h_p$, and thus the potential for significant entrainment relative to the total area of the plume is reduced, even for strong winds.

In the final state, where the isopycnals are nearly vertical (Fig. 2), the final area offshore of the initial value of W_α is

$$A_{o*} = \frac{1}{2}\frac{(h_{p*}^2 - h_p^2)}{\alpha} \qquad (16)$$

in which h_{p*} is the final depth of the plume. Hereafter, we use asterisk superscripted quantities for all plume scales in the final state. Now, the final depth is given by

$$h_{p*} = h_p\left(1 + \frac{\alpha}{\gamma} + 2\frac{\alpha A_e}{h_p^2}\right)^{1/2}, \qquad (17)$$

where A_e is the total amount of ambient water entrained into the plume during the wind event. If the evolution of the plume after the initial mixing is dominated by advective steepening of the isopycnals and there is no further entrainment of water into the plume (i.e., $A_e = A_{\gamma e} - A_\gamma$), it follows from volume conservation that $A_{\gamma e} = A_{o*}$. The final depth of the plume can then be derived by equating Eqs. (16) and (12) and solving for h_{p*}:

$$h_{p*} = \begin{cases} h_p\left[1 + \dfrac{\alpha}{\gamma}\left(1 + \dfrac{\delta_e^2}{h_p^2}\right)\right]^{1/2} & \text{for} \quad \delta_e < h_p \\[2ex] h_p\left[2\dfrac{\delta_e}{h_p}\left(1 + \dfrac{\alpha}{\gamma}\right) - \dfrac{\delta_e^2}{h_p^2}\right]^{1/2} & \text{for} \quad h_p \le \delta_e \le h_f \end{cases}, \qquad (18)$$

and, as hinted above, for $W_\gamma/W_\alpha \ll 1$ (bottom-trapped plumes) $h_{p*} \approx h_p$ even for strong winds. Thus, in this model the depth and width of bottom-trapped plumes are relatively insensitive to downwelling-favorable wind forcing. The fundamental reason is that the depth change that is attainable through entrainment and advective steepening is small relatively to the overall depth of a bottom-trapped plume.

To understand the evolution of the density field, we can use buoyancy conservation for the initial and final states of the plume. First we integrate $(\rho_0 - \rho)$ over the initial plume area to obtain

$$\int_0^{W_p}\int_{-h}^0 (\rho_0 - \rho)\,dz\,dx = \int_0^{W_p}\int_{-h}^0 \Delta\rho_c\left(1 - \frac{x - z/\gamma}{W_p}\right)dz\,dx$$

$$= \frac{\Delta\rho_c}{6W_p}\left[h_c W_\alpha^2\left(3 + 3\frac{W_\gamma}{W_\alpha} + \frac{\alpha}{\gamma} + \frac{W_\gamma^2}{W_\alpha^2}\right)\right.$$

$$\left. + \alpha W_\alpha^3\left(1 + \frac{W_\gamma}{W_\alpha}\right)^2\right] \qquad (19)$$

$$= \frac{\Delta\rho_c}{6}\alpha W_\alpha^2\left(1 + \frac{W_\gamma}{W_\alpha}\right) \quad \text{for} \quad h_c = 0. \qquad (20)$$

In the final state, where the isopycnals are nearly vertical and $W_{\gamma*} \approx 0$, the density can be written as $\rho_* = \rho_{c*} + (\Delta\rho_{c*}/W_{p*})x$ and the above equation is reduced to

$$\int_0^{W_{p*}}\int_{-h}^0 (\rho_0 - \rho_*)\,dz\,dx = \frac{\Delta\rho_{c*}}{6}(3h_c W_{p*} + \alpha W_{p*}^2) \qquad (21)$$

$$= \frac{\Delta\rho_{c*}}{6}\alpha W_{p*}^2 \quad \text{for} \quad h_c = 0. \qquad (22)$$

Using the above equation and the equation for the final depth of the plume we can estimate the final density difference from the initial conditions:

$$\Delta\rho_{c*} = \Delta\rho\frac{h_p^2}{h_{p*}^2}\frac{(1 - h_c/h_p)^2}{(1 + h_c/h_{p*} - 2h_c^2/h_{p*}^2)}\frac{1}{(1 + W_\alpha/W_\gamma)} \qquad (23)$$

$$\times \left[\frac{h_c}{h_p - h_c}\left(3 + 3\frac{W_\gamma}{W_\alpha} + \frac{\alpha}{\gamma} + \frac{W_\gamma^2}{W_\alpha^2}\right) + \left(1 + \frac{W_\gamma}{W_\alpha}\right)^2\right] \qquad (24)$$

$$= \Delta\rho_c\frac{h_p^2}{h_{p*}^2}\left(1 + \frac{W_\gamma}{W_\alpha}\right) \quad \text{for} \quad h_c = 0, \qquad (25)$$

where $W_{p*} \approx W_{\alpha*} = (h_{p*} - h_c)/\alpha$ is the final width of the plume. As hinted by the equation for the final depth, the change in density difference is also dependent on the

initial geometry of the plume. For bottom-trapped plumes, $h_p \approx h_{p*}$ and thus the density anomaly does not change significantly, even for strong winds. Taken together, the above equations can be used to predict the final geometry and buoyancy difference of the plume using the initial and forcing conditions.

An important part of the response is the acceleration of the along-shelf flow. In the final state, the effect of wind stress forcing on the along-shelf transport can be conceptualized as having two components (Whitney and Garvine 2005; Lentz and Largier 2006). First, there is the spinup of a geostrophic, barotropic alongshore flow, which can be approximated as

$$Q_w = \frac{\tau}{r\rho_o} A_{p*} \qquad (26)$$

where $A_{p*} = 1/2 W_{p*}(h_{p*} + h_c)$ is the final cross-sectional area of the plume and r is a linear bottom drag coefficient. The wind also mixes and deepens the plume, which results, overall, in an increased baroclinic transport. Assuming a 1½-layer model for the later component (see section 2a), the final transport is

$$Q_{p*} = \frac{g_*' h_{p*}^2}{6f} + \frac{\tau}{r\rho_o} A_{p*} \qquad (27)$$

$$= \frac{g_*' h_{p*}^2}{6f}\left[1 + \frac{u_w}{u_g}\left(1 - \frac{h_c^2}{h_{p*}^2}\right) + \frac{h_c}{\alpha W_{p*}}\left(1 + \frac{h_c^2}{h_{p*}^2}\right)\right] \qquad (28)$$

$$= \frac{g_*' h_{p*}^2}{6f}\left(1 + \frac{u_w}{u_g}\right) \quad \text{for} \quad h_c = 0, \qquad (29)$$

where u_w/u_g can be thought as a ratio of a wind-driven barotropic velocity $[u_w = \tau/(r\rho_o)]$ and a baroclinic velocity scale $[u_g = g_*'\alpha/(3f)]$ (for a similar reasoning, see Whitney and Garvine 2005). When the winds are relatively weak, the transport can be approximated by the final depth and density anomaly.

A reasonable time scale for the steepening process is given by

$$t_a = \frac{A_\gamma(1 + \alpha/\gamma)}{U_e(2 + \alpha/\gamma)}, \qquad (30)$$

which reduces to $t_a = A_\gamma/(2U_e)$ for $\alpha/\gamma \ll 1$, where $U_e = \tau/(\rho f)$ is the Ekman transport in the cross-shelf direction. This scale represents the time it takes for the cross-shore Ekman circulation to steepen the isopycnals, which depends on both the frontal (γ) and bottom (α) slopes. For relatively strong winds (or small plumes) this

time scale can be of the same order as the mixed layer spinup [Eq. (10)], namely, $1/f$. To incorporate this time dependence into the theory, we assume a linear increase in the mixed layer depth for times shorter than the mixed layer spinup time, such that

$$\delta_e = \begin{cases} \left(\dfrac{f}{N}\dfrac{\tau}{\rho_0}\right)^{1/2} t_a & \text{for} \quad t_a \lesssim f^{-1} \\ \dfrac{1}{(Nf)^{1/2}}\left(\dfrac{\tau}{\rho_0}\right)^{1/2} & \text{for} \quad t_a > f^{-1} \end{cases}. \qquad (31)$$

It is important to note that buoyant plumes can have a sharp frontal structure separating the ambient water from the fresh coastal water and is not constantly stratified as assumed here. The role that this variability plays in the transport and propagation properties of the plumes is explored in Pimenta et al. (2011), although at least some relatively small (Lentz and Largier 2006) and large (Moffat et al. 2008) coastal plumes can be approximated this way. Moreover, a key underlying assumption is that the along-shelf variability of the plume structure will not change significantly during the event, an assumption that should be tested carefully when contrasting the theory presented here against observations.

3. A two-dimensional numerical model of the wind-driven response

a. Numerical model description and setup

To test of the theory developed in the previous section, we use results from a series of numerical model runs. The Regional Ocean Modeling System (ROMS) is a widely used, primitive equation, open source numerical model. The model is terrain following, includes a free surface, and is hydrostatic (Shchepetkin and McWilliams 2005). Here we run the model in a two-dimensional configuration using periodic boundary conditions in the along-shelf direction. We define x as the cross-shelf direction, positive offshore, and z the vertical dimension, with zero at the undisturbed surface and positive upward (Fig. 1). The model domain is 50 km in the cross-shelf direction and has a horizontal resolution of 0.5 km. The coastal bathymetry is approximated by a small ($h_c = 5$ m) vertical wall at the coast and constant bottom slope α, which is either 10^{-3} (gentle slope) or 5×10^{-3} (steep slope). A wall is used at the offshore boundary. Making the domain wider while maintaining the horizontal resolution did not change the results in any significant way. In the vertical, the setup includes 25 levels, which results in an interior vertical resolution of ~2 m or better within the plume

TABLE 1. Initial conditions used to run the numerical model and forced with wind stress $\tau = -0.01, -0.05, -0.10, -0.50,$ and -1.00 N m^{-2}.

Run	h_p (m)	W_α (km)	W_γ (km)	$\Delta\rho_c$ (kg m^{-3})	$(-)Q$ (m^3 s^{-1})	α ($\times 10^{-3}$)
1	9.0	4.0	3.1	1.02	1547	1
2	14.8	2.0	4.2	0.63	1242	5
3	8.8	3.8	6.4	3.19	4322	1
4	12.9	1.6	7.2	2.38	3884	5
5	8.7	3.7	8.7	5.30	6981	1
6	12.1	1.4	9.0	4.27	6415	5
7	14.6	9.6	2.4	1.34	5582	1
8	19.2	2.8	4.6	0.92	4606	5
9	14.4	9.4	5.5	4.06	16 487	1
10	17.7	2.5	8.0	3.15	13 819	5
11	14.4	9.4	7.8	6.77	26 824	1
12*	17.3	2.5	10.0	5.31	23 367	5
13	18.9	13.9	2.2	1.41	9446	1
14	22.7	3.5	4.7	1.08	8168	5
15	18.6	13.6	5.3	4.25	28 516	1
16*	22.0	3.4	8.3	3.29	24 525	5
17	18.6	13.6	7.6	7.08	47 133	1
18*	21.7	3.3	10.6	5.37	41 388	5
19	27.7	22.7	2.0	1.47	19 688	1
20	30.4	5.1	5.0	1.21	18 461	5
21	27.3	22.3	5.1	4.41	60 262	1
22*	30.4	5.1	9.1	3.47	55 345	5
23*	27.2	22.2	7.6	7.35	101 691	1
24*	30.8	5.2	12.1	5.12	93 405	5

* Run for which t_a for $\tau = -0.01$ N m^{-2} is longer than 7 days, so it is not considered in the analysis.

for all model runs. Vertical resolution is higher near the surface and bottom. The model is run using the Mellor–Yamada turbulence closure scheme (Mellor and Yamada 1982), and the bottom stress is parameterized using a linear formulation with a coefficient $r = 5 \times 10^{-4}$ m s^{-1}.

The model is initialized with a plume with constant stratification [Eq. (1)], a density anomaly $\Delta\rho_c = \rho_o - \rho_c$, width W_α, and plume depth h_p. The frontal width W_γ is calculated using Eq. (4), and a velocity field in geostrophic balance with the density field is used to initialize the alongshore velocity field. The temperature in the model is set to 10°C everywhere, and the buoyancy anomaly of the plume is therefore accomplished by setting relatively freshwater with respect to an ambient salinity of 32 psu. The Coriolis parameter is set to $f = 10^{-4}$ s^{-1}. To fully explore the theory developed in section 2, we conducted 120 model runs, spanning a wide range of initial and forcing conditions for the fundamental parameters of the system, W_γ/W_α and δ_e/h_p (Table 1). Prior to simulating the response to wind stress forcing, the model is run unforced for several days, which allows transients to decay. On day 10 of each model run, a constant, downwelling-favorable wind stress is applied

for 10 days, a reasonable choice given our focus on synoptic-scale forcing variability.

Given our choice of initial conditions, the model runs result in 24 distinct initial states, which we use to test the theoretical predictions for the initial scales (section 2a). Figure 3 illustrates the initial conditions of salinity (top panels) and alongshore velocity (bottom panels) for a bottom-trapped, intermediate, and surface-trapped plume. For each run, the initial geometry of the plume is obtained by using an isohaline whose value is the ambient salinity (32) minus 10% of the overall salinity difference of the plume. That is, if the initial surface salinity anomaly (ambient salinity minus the surface salinity at the coast) is 5, the reference isohaline for the entire run would be 31.50 psu. Overall, the reference isohaline ranged from 31.05 to 31.90 psu. The volume transport of the plume is calculated by integrating the alongshore velocity component shoreward of the location of that reference isohaline. The density anomaly is calculated as the difference between ambient and surface density at the coast. Figure 4 shows a comparison between the predicted and modeled plume width and depth for day 9 of all model runs, prior to wind forcing. The scale for the width [Eq. (4)] is shown multiplied by a constant $c = 1.2$. After several days of adjustment, the plume has reached a geostrophic balance in the cross-shelf momentum balance, which results, as expected, in the good agreement between the theory and the model output.

b. Evolution of key plume scales during a wind event

To illustrate the basic structure of the response of a plume to downwelling-favorable wind stress forcing, we show, in Fig. 5, a case forced by relatively weak wind stress forcing. By day 9, the plume is 8.7 m deep, with a surface buoyancy anomaly of 5.3 kg m^{-3}. The frontal width is approximately 8.7 km, which results in a width ratio of $W_\gamma/W_\alpha = 2.4$. The wind forcing is -0.01 N m^{-2}, which, given the plume stratification, means that the forcing ratio δ_e/h_p is about 0.14. Figure 5 shows the evolution of the wind-driven event over several days.

After the wind stress starts, the surface quickly becomes mixed throughout the domain, as evidenced by the nearly vertical isopycnals at the surface (Fig. 5, top). A surface Ekman layer spins up and the surface water starts to be advected shoreward. Offshore of the plume front, the surface and bottom Ekman layers become increasingly distinct from each other as the bottom deepens. Onshore of the front, the Ekman layers are thinner as a consequence of the plume stratification. As a result of the steepening isopycnals, which increases the geostrophic shear, and the increase of the surface slope, the alongshore flow accelerates significantly over the duration of the event.
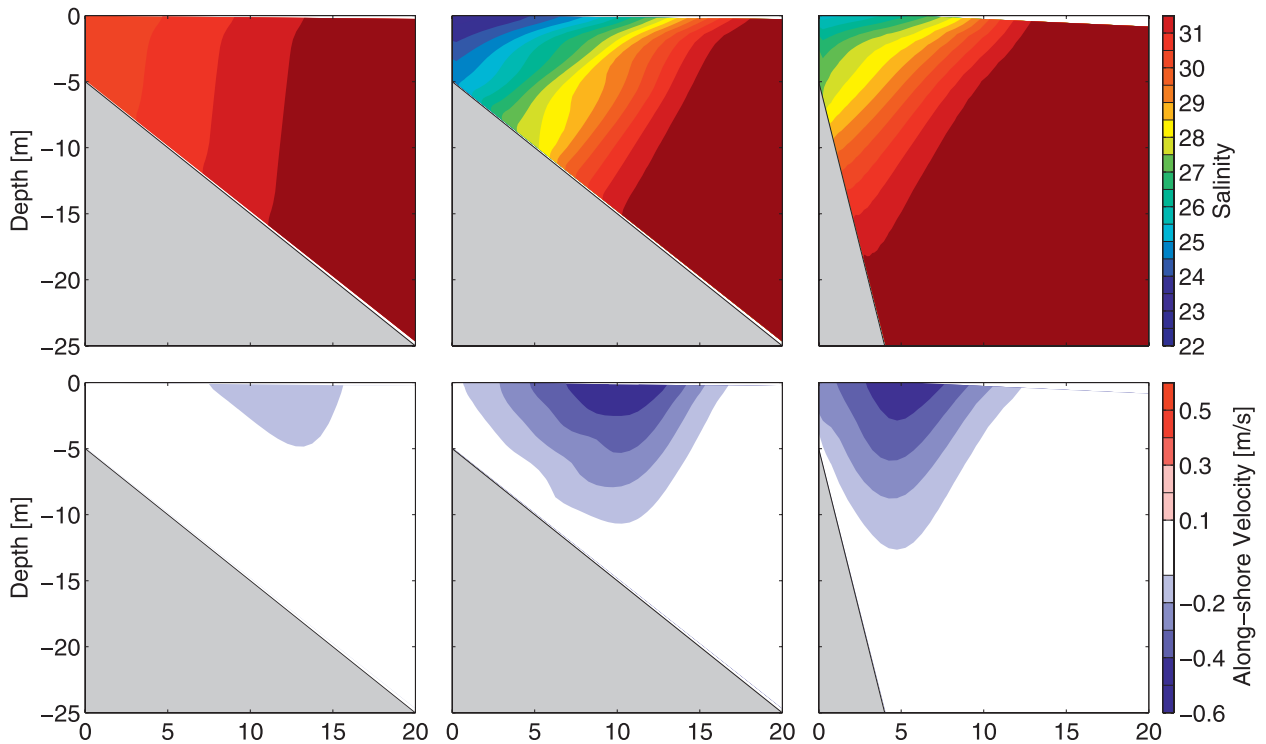
FIG. 3. Initial salinity and alongshore velocity for (left) a bottom-trapped (run 13), (middle) an intermediate (run 11), and (right) a surface-trapped (run 12) plume.

The development of the cross-shelf circulation offshore of the plume resembles the response expected for an unstratified shelf, with surface and bottom Ekman layers clearly distinguishable at the offshore edge of the right panels of Fig. 5 (see in particular the streamfunction) but merging together onshore. The cross-shore divergence of the Ekman transport leads to downwelling just offshore of the plume front, which consist by this point of nearly vertical isopycnals. The resulting along-shelf transport has increased considerably. As for the cross-shelf circulation, the vertical shear within the plume causes a response that is clearly distinct compared to the region
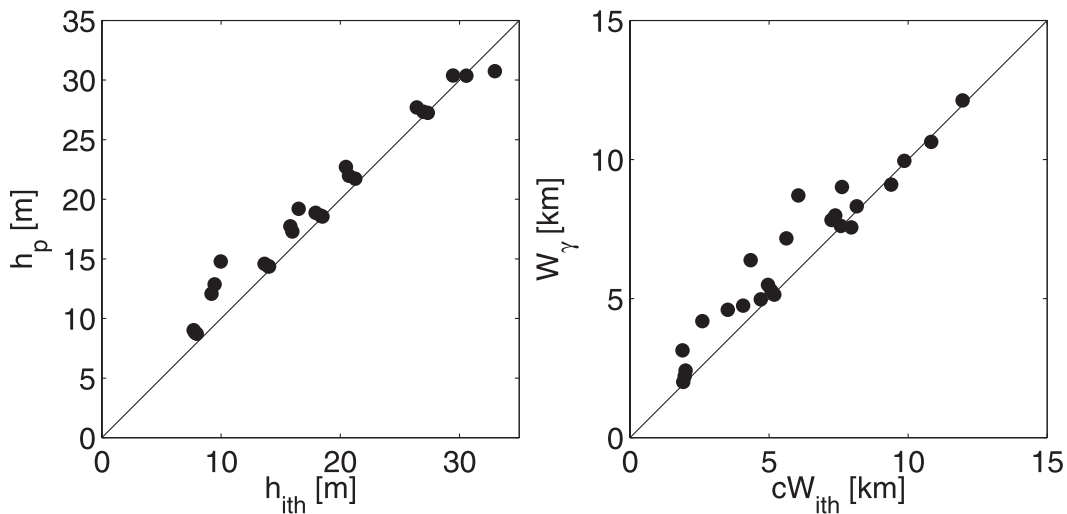
FIG. 4. Initial (left) plume depth and (right) frontal area width from the numerical model (vertical axis) vs the theoretical predictions (horizontal axis, with subscript ith). The theoretical width is scaled by a constant $c = 1.2$.
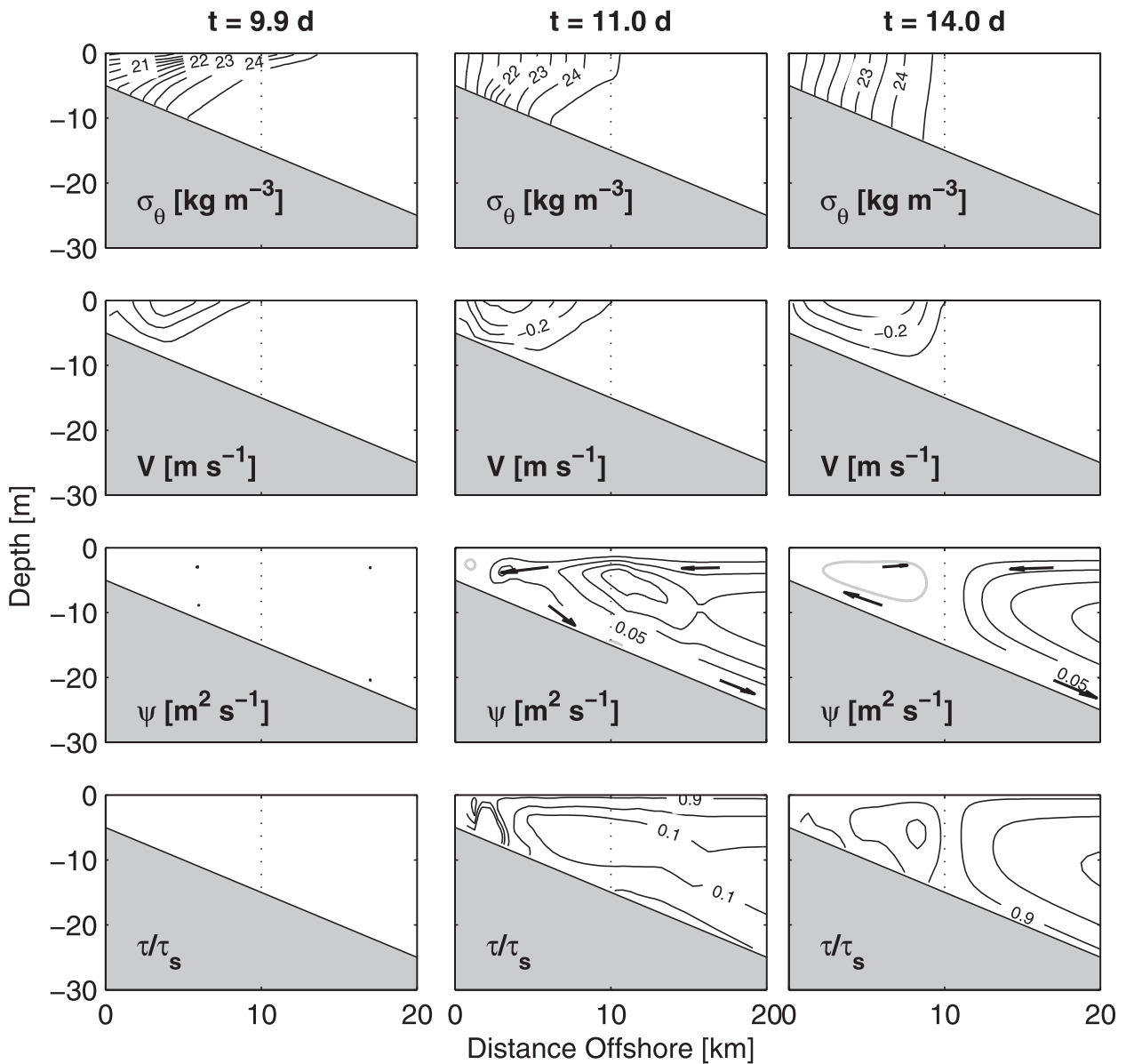
FIG. 5. Evolution of the potential density (σ_θ), along-shelf velocity (v), streamfunction (ψ) and normalized stress (τ_i/τ, where τ_i is the internal stress) for model run 5 (left) as the wind forcing ($\tau = -0.01$ N m^{-2}) begins, (middle) 24 h after, and (right) 96 h after. Gray (black) solid streamlines indicate clockwise (anticlockwise) circulation in the z–x plane. A vertical dotted line at $x = 10$ km is added for reference.

offshore of the plume (or what it would be in the absence of stratification). The region offshore of the plume shows a weak recirculation with a sense opposite to the circulation offshore of the front, which reinforces the surface convergence (divergence) at the surface (bottom) on the offshore edge of the plume. The conditions for the formation of this reverse circulation near the shore are explored in the discussion.

Figure 6 shows the evolution of the key scales of the plume during the event. Clearly, the largest changes in

the plume buoyancy anomaly and transport occur as the plume deepens and narrows; that is, when the initial mixing occurs, the barotropic wind response is spun up and the plume undergoes advective steepening. Because the entrainment of ambient water into the plume increases its volume, the steepening process results in more deepening and less narrowing than with advective steepening alone. Although the theory only includes the evolution up to the point where the isopycnals are nearly vertical (just after day 13 in the run shown in Fig. 6), it is
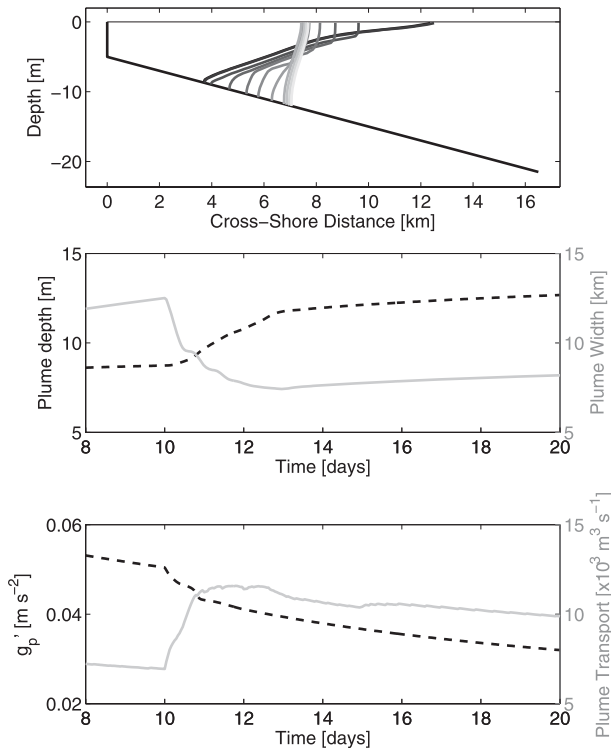
FIG. 6. (top) Evolution of the front of the plume ($S = 31.95$ psu) for case 5 forced with a wind stress $\tau = -0.01$ N m^{-2}. The darkest line corresponds to the time just prior to the unset of the wind, and the increasingly lighter ones are snapshots of the isohaline every 12 h. Also shown are (middle) the plume depth and width and (bottom) the reduced gravity and transport.

clear that this state is not completely steady, and the plume continues to slowly widen, deepen, and become more mixed (the transport is reduced slightly throughout the event) as frontal processes continue to entrain ambient water along the front. However, and as assumed in the theory, the major changes in plume geometry and other properties occur during the early mixing and steepening process.

The evolution of the scales during the event shows that, after the initial spinup of the Ekman circulation, the plume narrows at progressively slower rates. This can be readily understood by considering that, as the plume isopycnals are advected onshore, the mixed layer thickens and thus the average velocity within the Ekman layer is reduced. This behavior is analogous to the offshore motion of a downwelling front on a shelf with constant slope and starting from rest (Austin and Lentz 2002), with the bottom slope in that case replaced by the frontal slope here.

c. Comparing the theoretical predictions to the model results

The theory derived in section 2 provides predictions for the final depth, width, density anomaly, and along-shelf transport for a plume forced by constant wind. Model runs spanning a wide range of initial and forcing conditions (Table 1) were analyzed to test these predictions. Initial conditions were taken at $t = 9.75$ days, and final scales are taken at $t = 17$ days. Six runs that do not reach the final state in those seven days (i.e., $t_a > 7$ days) when forced with the weakest stress (0.01 N m^{-2}) are not considered in the analysis. After discarding those runs, 114 remain for comparison with the theory.

Comparison for theoretical predictions against numerical model results is shown in Fig. 7. The predictions are, overall, reasonable (Table 2). For event time scales t_a shorter than the spinup period $t_i = 1/f$, the theory tends to do well. When the time it takes for the isopycnals to become vertical due to advection is long compared to the spinup time (black circles in Fig. 7), the theoretical predictions comparison to the model results are worse. The predicted changes for the density difference are poorer than for other plume properties, an indication of the importance of entrainment processes not considered in our simplified model.

The dependency of the response to the initial geometry of the plume and the intensity of the wind forcing is illustrated in Fig. 8. The left panel shows the normalized plume depth as a function of α/γ. The curves are the theoretical predictions for $\delta_e/h_p = 0.06$–0.2 (black curves) and 0.4–0.6 (gray curves). The dots and squares are the numerical model results whose initial conditions fall within each range of δ_e/h_p (the color of the symbols match each curve). As predicted by the theory, increasingly bottom-trapped plumes ($\alpha/\gamma \ll 1$) show little relative deepening, regardless of wind strength and initial stratification. As the plume becomes surface trapped, the deepening is significant, with the plume deepening to maximum values of more than twice its initial depth for the initial geometry and forcing conditions chosen here.

The model results shown, however, do not fit well the expected dependency on the forcing ratio (δ_e/h_p). The theory presented was unsatisfactory to correctly account for the entrainment over the parameter considered. Reasons for the disagreement include the continuous entrainment of ambient water during the advective steepening process (particularly for weak winds); the entrainment process being less efficient that assumed (for strong winds); and the continuous evolution after the isopycnals first become nearly vertical, which the theory ignores. This issue is explored further in the discussion.

A similar picture arises from examination of the dependency of the normalized width (including a factor ϵ involving h_c) as a function of the width ratio W_γ/W_α. Bottom-trapped plumes suffer little change of width as a result of the wind forcing, whereas surface-trapped plumes undergo the largest relative narrowing. However,
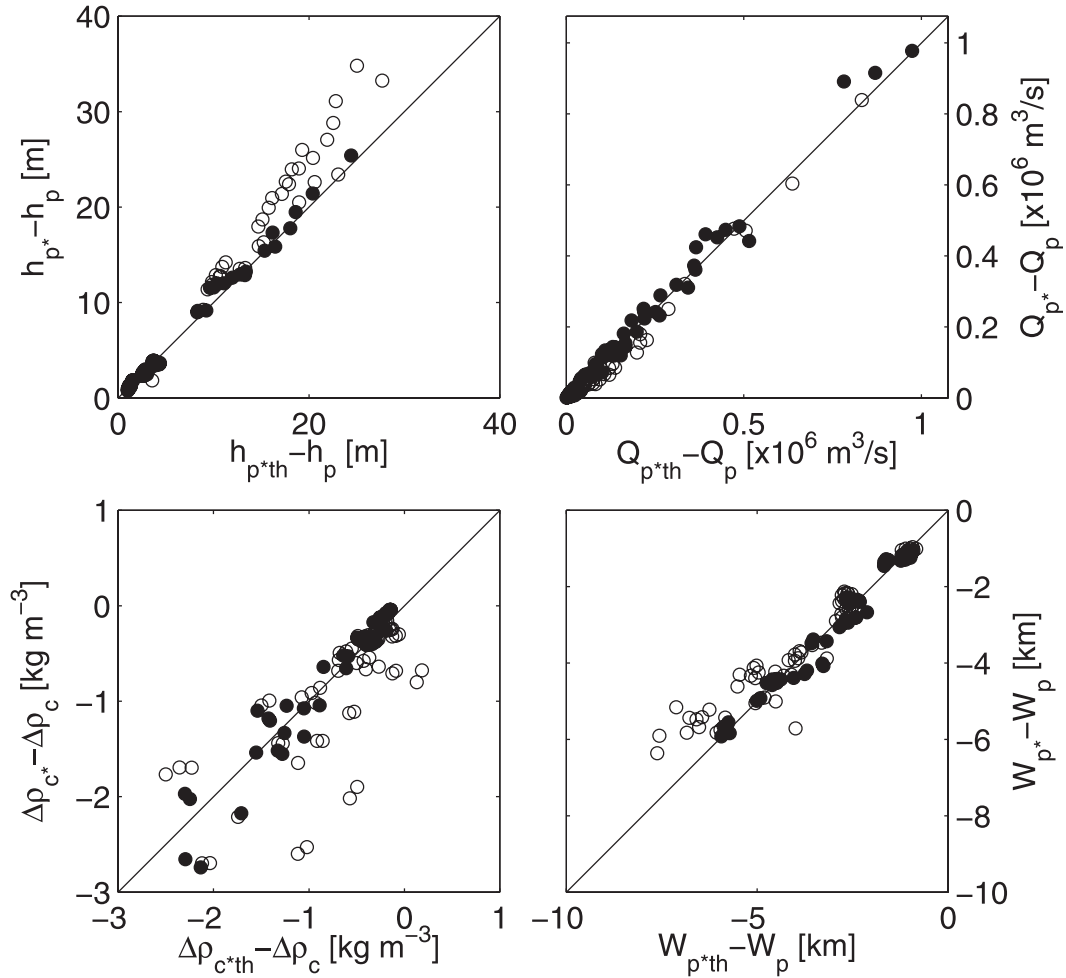
FIG. 7. Comparison between the numerical model output and theoretical predictions for (top left) the total deepening, (top right) change in the along-shelf transport, (bottom left) change in density anomaly, and (bottom right) total narrowing during an event. For all panels, open (solid) circles correspond to cases where $t_d/t_i \leq 1$ ($t_d/t_i > 1$).

as expected from the analysis of evolution of the depth scale, the entrainment processes involved in these events cannot be accounted by the simple approximation used in our theory.

Overall, the theory provides a reasonable first-order prediction of the resulting scales from a downwelling-favorable wind event forcing a coastal buoyant plume. The initial conditions used in the numerical model are relevant for many midlatitude coastal buoyant plumes. A few issues of interest related to this work, as well as its shortcomings, are discussed in the next section.

4. Discussion

a. Evolution of the entrainment

Although the theoretical model and numerical model results show reasonable agreement, the former assumes a simplified entrainment model that does not capture the

complexity of the evolution of the plume during a wind event. Figure 9 illustrates some of the key mixing processes occurring during an event. The top three panels show the gradient Richardson number [$\mathrm{Ri} = N^2/(du/dz^2 + dv/dz^2)$] and the along- and cross-shore velocity shear evolution with time for the plume frontal region. Each property is measured along the frontal isohaline, and their projected distance over the cross-shelf axis is

TABLE 2. Correlation coefficients and slopes for the theory and numerical model results comparisons shown in Fig. 7, for $t_d/t_i \leq 1$ ($t_d/t_i > 1$). All results have a p value <0.005.

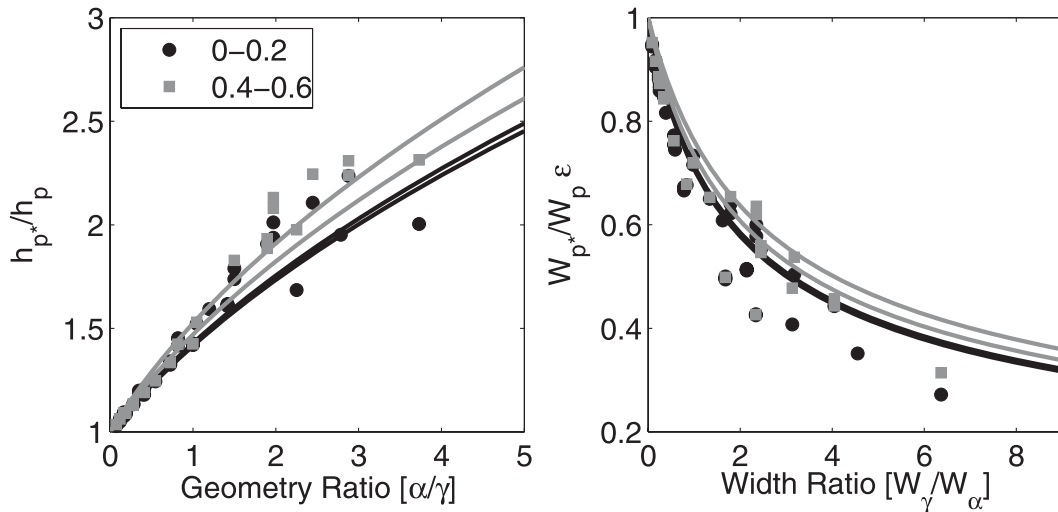| Property	R	Slope
$h_{p*} - h_p$	0.96 (0.99)	0.82 ± 0.04 (1.27 ± 0.02)
$\Delta\rho_{c*} - \Delta\rho_c$	0.91 (0.77)	0.72 ± 0.05 (0.89 ± 0.09)
$Q_{p*} - Q_p$	0.98 (0.99)	0.96 ± 0.03 (0.97 ± 0.01)
$W_{p*} - W_p$	0.80 (0.95)	0.77 ± 0.09 (0.81 ± 0.03)

FIG. 8. (left) Plume depth at $t = 17$ days normalized by initial value (at $t = 9.5$ days) as a function of the geometry ratio α/γ and (right) normalized plume width as a function of the width ratio W_γ/W_α. The black (gray) color corresponds to a range of forcing ratio (δ_e/h_p) of 0.06–0.2 (0.4–0.6). The factor $\epsilon = (1 - h_c/h_p)/(1 - h_c/h_{p*})$ arises from having a vertical wall at the coast, and it ranges from 0.71 to nearly 1. The symbols correspond to the numerical model runs, and the solid lines correspond to the theory predictions (one curve for each extreme of each range of forcing ratio).

plotted on the y axis of these panels. As expected, much of the shear leading to critical values of the Richardson number occur primarily near the surface, with high values occurring near the bottom as the return flow spins up. Notice that, as the event progresses, the projected length

of the isohaline is reduced as the mixing and Ekman circulation sharply steepen the density field.

Figure 9 (bottom) shows the rate of change of the plume area as well as evolution of the depth. The largest change in area occurs shortly after onset of the wind,
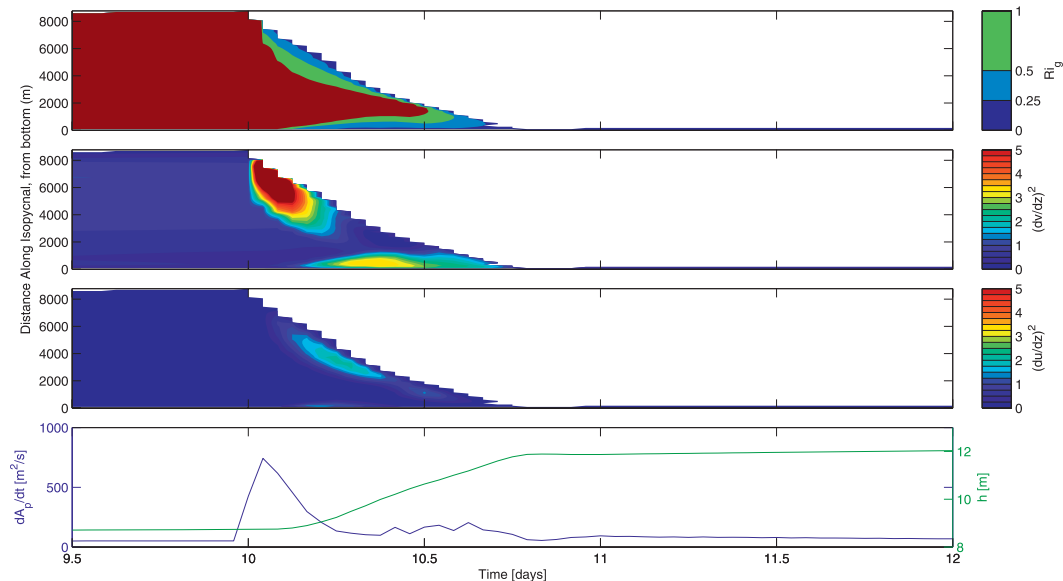

FIG. 9. Evolution of (top) the gradient Richardson number, (upper middle) along- and (lower middle) cross-shore velocity gradient squared, and (bottom) change of plume area and plume depth for run 5 forced with $\tau = -0.05$ N m^{-2}. (top)–(bottom middle) The corresponding variables in the top three panels are shown as a function of the distance along the reference salinity for the run; that is, the height of the colored area represents the projected length of the isohaline at a given time (which is reduced as the plume narrows and deepens forced by the wind).
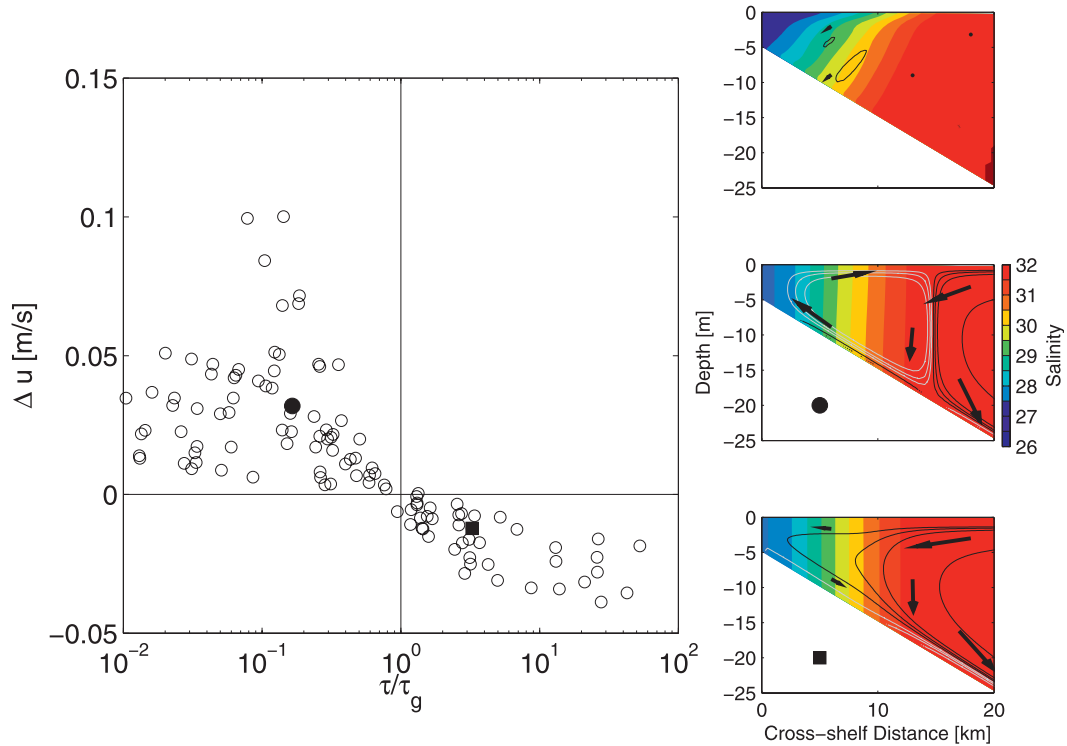
FIG. 10. Influence of the geostrophic shear on the cross-shelf circulation. (left) The top-to-bottom difference in the cross-shelf velocity (positive values indicate clockwise circulation in the x–z plane) as a function of the ratio of the geostrophic (τ_g) to wind (τ) stress for all events after seven days of forcing. Prior to the start of the wind (top right panel) the cross-shelf circulation is extremely weak. When $\tau < \tau_g$ (middle right panel), there is strong surface convergence and oceanward (shoreward) surface (bottom) flow associated with the plume. A much weaker circulation in the same sense as offshore of the plume is evident in the model for $\tau > \tau_g$ (bottom right panel).

associated mainly with the increased surface shear, as assumed in the theory. Notice that the deepening does not occur at this stage but when the bottom return flow is developed. Clearly, there is entrainment of ambient water after the initial entrainment, and both across- and alongshore vertical shears seem to contribute to this process. Other events (not shown) show a similar pattern of high values of entrainment (as measured by areal changes) early in the process, which are associated with inertial-scale shear variability [for a similar discussion for the upwelling-favorable case, see Fong and Geyer (2001)]. Future inclusion of these more complex entrainment processes on the surface and bottom in the theory are likely to improve the predictions presented in the previous section.

b. Cross-shelf circulation

In the absence of buoyant water at the coast, the cross-shelf circulation during a downwelling-favorable wind event is characterized by onshore flow at the surface and a return flow at depth (Allen and Newberger 1996; Austin and Lentz 2002). As the surface and bottom boundary layers converge toward the coast, the cross-shelf

circulation weakens. However, as shown in section 3b, the plume cross-shelf circulation during a downwelling-favorable wind event can result in oceanward flow at the surface and shoreward flow at the bottom. This creates surface convergence (and bottom divergence) of the circulation at the offshore edge of the plume.

This reversal of the near-shore circulation reveals the influence of the lateral density gradient and accompanying vertical geostrophic shear in the buoyancy and momentum balances. The stress associated with the geostrophic shear can induce an Ekman circulation in the opposite sense if it becomes larger than the surface wind stress. Otherwise, the circulation is qualitatively similar to the case where no buoyant water is found at the coast. A rough scaling for this geostrophic shear is, from the bulk formula for the surface stress, $\tau_g = \rho_o C_d v_g^2$, where $v_g = \rho_o^{-1} g\ (\Delta\rho_{c*}/W_{p*})(h_{p*}/f)$ is an estimate of the geostrophic velocity during the event and C_d is a drag coefficient, here taken as 1.3×10^{-3}.

Figure 10 illustrates this competition and its effect on the cross-shore circulation. For $\tau/\tau_g > 1$, the cross-shelf circulation as a top-to-bottom velocity difference Δu at $x = W_{p*}/2$ after seven days of forcing (so that negative
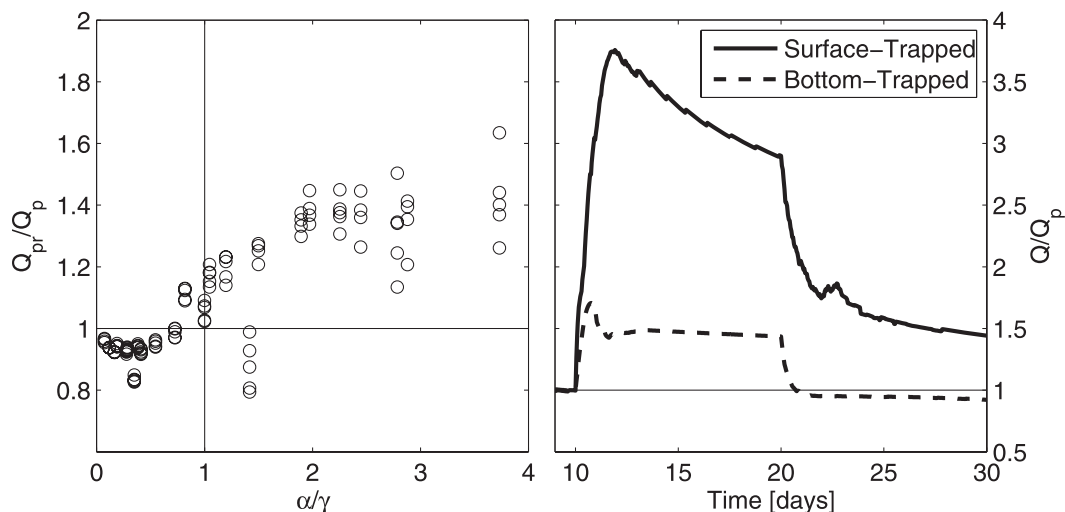
FIG. 11. (left) Alongshore transport measured 10 days after the relaxation of downwelling-favorable wind stress. (right) The evolution of the alongshore transport for a surface-trapped ($\alpha/\gamma > 1$, run 6 with $\tau = -0.05$ N m^{-2}, solid line) and a bottom-trapped ($\alpha/\gamma < 1$, run 7 with $\tau = -0.01$ N m^{-2}, dashed line) plume. In both panels the transport is normalized by the transport prior to the wind event (Q_p). For the right plot constant downwelling-favorable wind stress was maintained between days 10 and 20.

values represent an anticlockwise circulation in the x–z plane) is qualitatively as expected for a wind-driven response in a homogeneous ocean. For $\tau/\tau_g < 1$, however, the circulation is reversed. The intensity of the wind required for a circulation reversal can be readily calculated from the theoretical estimates of the plume geometry and density anomaly.

c. Transient wind forcing events

In the absence of wind forcing, the initial plume geometry is critical to understand the dynamics of propagation along the coast (Lentz and Helfrich 2002). Surface-trapped plumes ($W_\gamma/W_\alpha \gg 1$) propagate faster along the coast than bottom-trapped ones ($W_\gamma/W_\alpha \ll 1$) with the same depth and reduced gravity. Here we have shown that the initial geometry of the plume is also key to understand its response to downwelling-favorable wind stress forcing. In all cases, the wind stress forcing results in mixing, steepening of the isopycnals, and an increase of the along-shelf volume transport. However, bottom-trapped plumes suffer relatively little deepening, narrowing, and entrainment of ambient water compared to surface-trapped ones. Overall, the effect of downwelling-favorable wind stress forcing is to make relatively surface-trapped plumes more bottom trapped.

As shown in the previous section, bottom-trapped plumes are less sensitive to the forcing than surface-trapped plumes. This is also evident after the wind event ends. Figure 11 (left) shows the alongshore transport of

the plume for all numerical runs, after a 10-day wind event has ended and an additional 10 days have passed to allow for adjustment. The transport is normalized by its value prior to the start of the wind event. The time evolution of this normalized alongshore transport for a bottom-trapped and surface-trapped plume is also shown (Fig. 10, right). Surface-trapped plumes undergo stronger changes in geometry and density anomaly during the event, which results in a larger alongshore transport after the wind stops. Bottom-trapped plumes, on the other hand, show increased along-shelf transport during the event but relax to a state closely resembling the one prior to the start of wind forcing.

Finally, it is worth noting that the theory and numerical model results presented above make significant simplifications, which allows us to gain insight into key features of the response of a buoyant plume to wind forcing. However, the two-dimensional modeling approach does not allow us to consider interaction of the plume with the upstream region where the plume originates and where important processes take place (Garvine 2001; Horner-Devine 2009) or the possible role of along-shelf pressure gradients in the dynamics considered. We have also omitted the influence of tides in mixing and modifying the circulation of the plume (e.g., Horner-Devine et al. 2009). All of the above processes are likely to be important, individually or in combination, in most real systems, thus creating the potential for additional entrainment mechanisms and complicating the relatively simple circulation we have shown here. Our choice of a

simple forcing function is reasonable when considering wind events of short duration (thus our focus in the response in the first few days after the start of the forcing), but the role of time-varying winds and cross-shore winds are a natural extension of the work presented here.

5. Summary

Here, we have explored the response of a coastally trapped buoyant plume to downwelling-favorable wind stress. The largest changes in the plume geometry, density anomaly, and along-shelf transport occur as the isopycnals undergo strong steepening, which results in the plume isopycnals becoming nearly vertical. After this process ends, the plume continues to evolve as a limited amount of entrainment continues to increase the salinity of the plume, therefore causing it to deepen and widen.

The along-shelf transport of the plume increases as a result of a direct, barotropic wind-driven response and an indirect (but also wind-driven) steepening of the isopycnals, which results in increased baroclinic geostrophic transport. The cross-shelf velocity structure is characterized generally by convergence and downwelling at the offshore boundary of the plume as a result of a weakening of the cross-shelf exchange or the setup of a seaward (shoreward) flow at the surface (bottom) within the plume.

A simple theory, approximating the evolution as the initial entrainment of ambient water into the plume followed by the advective steepening of its isopycnals, provides reasonable predictions of the plume width, depth, and density difference. Further, assuming that the cross-shelf momentum balance is geostrophic and that the barotropic, direct wind-driven response can be linearly added to the baroclinic transport calculated from those scales also results in good agreement with the numerical model results.

The theory suggest that the response is critically dependent on the initial plume geometry through the width ratio W_γ/W_α and, to a lesser extent, to the forcing ratio of the Ekman layer to initial plume depth δ_e/h_p. Plumes that are initially bottom trapped ($W_\gamma/W_\alpha \ll 1$) will suffer relatively small depth and width changes as a result of downwelling-favorable wind stress events compared to a similar surface-trapped plume. The total amount of ambient water available for entrainment and the potential deepening and narrowing through advective steepening is relatively small for the former kind. The numerical model results revealed that the mixing model included in the theory is possibly too simplified.

Overall, the theory and numerical modeling results presented here provide a reasonably clear picture of the evolution of the geometry, density anomaly, and along-shelf transport of a buoyant plume subjected to downwelling-favorable wind stress forcing. Of equal importance, a relatively straightforward set of predictions that can be tested against observations, where the utility of the theory can be ultimately judged.

REFERENCES

Allen, J., and P. Newberger, 1996: Downwelling circulation on the Oregon continental shelf. Part I: Response to idealized forcing. *J. Phys. Oceanogr.,* **26,** 2011–2035.

Austin, J. A., and S. Lentz, 2002: The inner shelf response to wind-driven upwelling and downwelling. *J. Phys. Oceanogr.,* **32,** 2171–2193.

Avicola, G., and P. Huq, 2003: The characteristics of the recirculating bulge region in coastal buoyant outflows. *J. Mar. Res.,* **61,** 435–463, doi:10.1357/002224003322384889.

Chao, S., and W. Boicourt, 1986: Onset of estuarine plumes. *J. Phys. Oceanogr.,* **16,** 2137–2149.

Chapman, D., and S. Lentz, 1994: Trapping of a coastal density front by the bottom boundary layer. *J. Phys. Oceanogr.,* **24,** 1464–1479.

——, and ——, 1997: Adjustment of stratified flow over a sloping bottom. *J. Phys. Oceanogr.,* **27,** 340–356.

Fong, D., and W. Geyer, 2001: Response of a river plume during an upwelling favorable wind event. *J. Geophys. Res.,* **106** (C1), 1067–1084.

Garvine, R., 2001: The impact of model configuration in studies of buoyant coastal discharge. *J. Mar. Res.,* **59,** 193–225.

Geyer, W. R., P. Hill, T. Milligan, and P. Traykovski, 2000: The structure of the Eel River plume during floods. *Cont. Shelf Res.,* **20,** 2067–2093, doi:10.1016/S0278-4343(00)00063-7.

Gill, A., 1976: Adjustment under gravity in a rotating channel. *J. Fluid Mech.,* **77,** 603–621, doi:10.1017/S0022112076002280.

Hickey, B., S. Geier, N. Kachel, and A. MacFadyen, 2005: A bi-directional river plume: The Columbia in summer. *Cont. Shelf Res.,* **25,** 1631–1656, doi:10.1016/j.csr.2005.04.010.

——, and Coauthors, 2010: River influences on shelf ecosystems: Introduction and synthesis. *J. Geophys. Res.,* **115,** C00B17, doi:10.1029/2009JC005452.

Horner-Devine, A. R., 2009: The bulge circulation in the Columbia River plume. *Cont. Shelf Res.,* **29,** 234–251, doi:10.1016/j.csr.2007.12.012.

——, D. A. Jay, P. M. Orton, and E. Y. Spahn, 2009: A conceptual model of the strongly tidal Columbia River plume. *J. Mar. Syst.,* **78,** 460–475, doi:10.1016/j.jmarsys.2008.11.025.

Kourafalou, V., L. Oey, J. Wang, and T. Lee, 1996: The fate of river discharge on the continental shelf 1. Modeling the river plume and the inner shelf coastal current. *J. Geophys. Res.,* **101** (C2), 3415–3434.

Kudela, R. M., and Coauthors, 2008: New insights into the controls and mechanisms of plankton productivity in coastal upwelling waters of the Northern California current system. *Oceanography,* **21,** 46–59.

Lentz, S., 2004: The response of buoyant coastal plumes to upwelling-favorable winds. *J. Phys. Oceanogr.,* **34,** 2458–2469.

——, and K. R. Helfrich, 2002: Buoyant gravity currents along a sloping bottom in a rotating fluid. *J. Fluid Mech.,* **464,** 251–278, doi:10.1017/S0022112002008868.

——, and J. Largier, 2006: The influence of wind forcing on the Chesapeake Bay buoyant coastal current. *J. Phys. Oceanogr.,* **36,** 1305–1316.

——, R. Guza, S. Elgar, F. Feddersen, and T. Herbers, 1999: Momentum balances on the North Carolina inner shelf. *J. Geophys. Res.,* **104** (C8), 205–226.

McWilliams, J. C., E. Huckle, and A. F. Shchepetkin, 2009: Buoyancy effects in a stratified Ekman layer. *J. Phys. Oceanogr.,* **39,** 2581–2599.

Mellor, G., and T. Yamada, 1982: Development of a turbulence closure model for geophysical fluid problems. *Rev. Geophys.,* **20,** 851–875.

Moffat, C., R. C. Beardsley, W. B. Owens, and N. van Lipzig, 2008: A first description of the Antarctic Peninsula Coastal Current. *Deep-Sea Res. II,* **55** (3–4), 277–293, doi:10.1016/j.dsr2.2007.10.003.

Ogston, A., D. Cacchione, R. Sternberg, and G. Kineke, 2000: Observations of storm and river flood-driven sediment transport on the northern California continental shelf. *Cont. Shelf Res.,* **20,** 2141–2162, doi:10.1016/S0278-4343(00)00065-0.

Pimenta, F. M., A. D. Kirwan, and P. Huq, 2011: On the transport of buoyant coastal plumes. *J. Phys. Oceanogr.,* **41,** 620–640.

Pollard, R., P. Rhines, and R. Thompson, 1972: The deepening of the wind-mixed layer. *Geophys. Astrophys. Fluid Dyn.,* **4,** 381–404.

Rennie, S., S. Lentz, and J. Largier, 1999: Observations of a pulsed buoyancy current downstream of Chesapeake Bay. *J. Geophys. Res.,* **104** (C8), 18 227–18 240.

Shchepetkin, A. F., and J. C. McWilliams, 2005: The Regional Oceanic Modeling System (ROMS): A split-explicit, free-surface, topography-following-coordinate oceanic model. *Ocean Modell.,* **9,** 347–404, doi:10.1016/j.ocemod.2004.08.002.

Wang, B., 2006: Cultural eutrophication in the Changjiang (Yangtze River) plume: History and perspective. *Estuarine Coastal Shelf Sci.,* **69** (3–4), 471–477, doi:10.1016/j.ecss.2006.05.010.

Warrick, J. A., and Coauthors, 2007: River plume patterns and dynamics within the Southern California Bight. *Cont. Shelf Res.,* **27,** 2427–2448, doi:10.1016/j.csr.2007.06.015.

Whitney, M. M., and R. W. Garvine, 2005: Wind influence on a coastal buoyant outflow. *J. Geophys. Res.,* **110,** C03014, doi:10.1029/2003JC002261.

Wiseman, W. J., Jr., and R. W. Garvine, 1995: Plumes and coastal currents near large river mouths. *Estuaries,* **18,** 509–517, doi:10.2307/1352368.

Yankovsky, A., and D. Chapman, 1997: A simple theory for the fate of buoyant coastal discharges. *J. Phys. Oceanogr.,* **27,** 1386–1401.